Science Advances

AAAS

advances.sciencemag.org/cgi/content/full/4/3/eaar3219/DC1

Supplementary Materials for

Nanostructure, osteopontin, and mechanical properties of calcitic avian eggshell

Dimitra Athanasiadou, Wenge Jiang, Dina Goldbaum, Aroba Saleem, Kaustuv Basu, Michael S. Pacella, Corinna F. Böhm, Richard R. Chromik, Maxwell T. Hincke, Alejandro B. Rodríguez-Navarro, Hojatollah Vali, Stephan E. Wolf, Jeffrey J. Gray, Khanh Huy Bui, Marc D. McKee

Published 30 March 2018, *Sci. Adv.* **4**, eaar3219 (2018)
DOI: 10.1126/sciadv.aar3219

The PDF file includes:

Other Supplementary Material for this manuscript includes the following:
(available at advances.sciencemag.org/cgi/content/full/4/3/eaar3219/DC1)

- movie S4 (.mov format). 3D reconstruction of a nanostructured region found in the synthetic calcite crystal grown with 5.9 μM OPN.

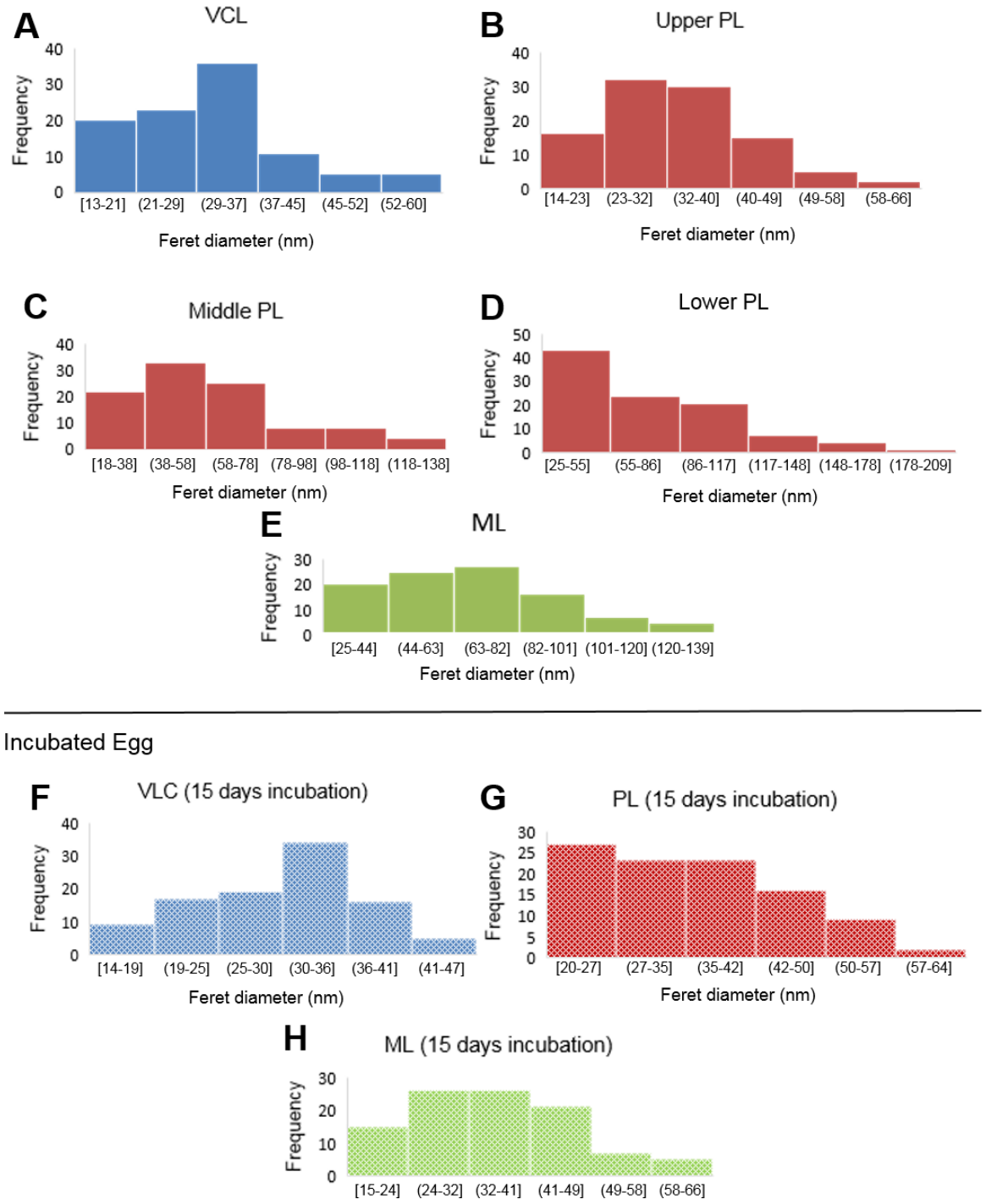

fig. S1. Distribution of measured eggshell nanostructures by AFM. (**A-E**) Distribution of nanostructure size from VCL (A), upper PL (B), middle PL (C), lower PL (D) and ML (E) layers of the eggshell. (**F-H**) Distribution of nanostructure size from VCL (F), lower PL (G) and ML (H) of an egg incubated for 15 days.

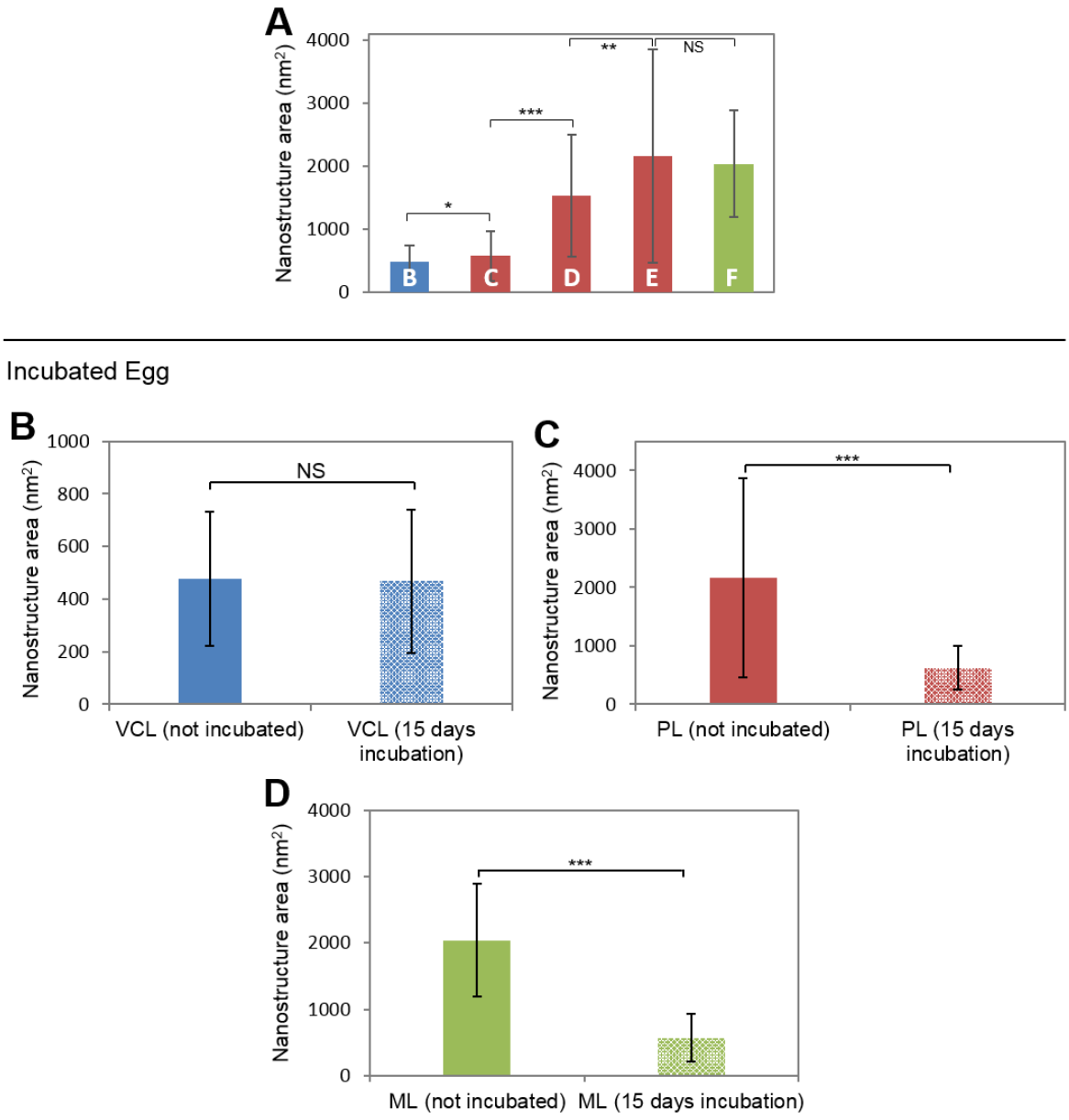

fig. S2. Eggshell nanostructure area measurements. (**A**) Histogram of nanostructure area distribution in the VCL (**B**), upper PL (**C**), middle PL (**D**), lower PL (**E**) and ML (**F**) (see Fig. 1A for identification of these layers). Significant difference indicated by brackets (*p<0.05, **p<0.01 and ***p<0.001). No significant difference (NS) (p>0.05) between bars E and F. Nanostructure area distribution in eggshell VCL (B), PL (C) and ML (D) comparing eggs that were not incubated to incubated eggs. No significant difference (p>0.05) is observed between vertical crystal layers, whereas a significant difference (***p<0.001) in area exists between the two groups for the palisades layer, and for the mammillary layer. Values were compared by a two-paired Student's *t*-test.

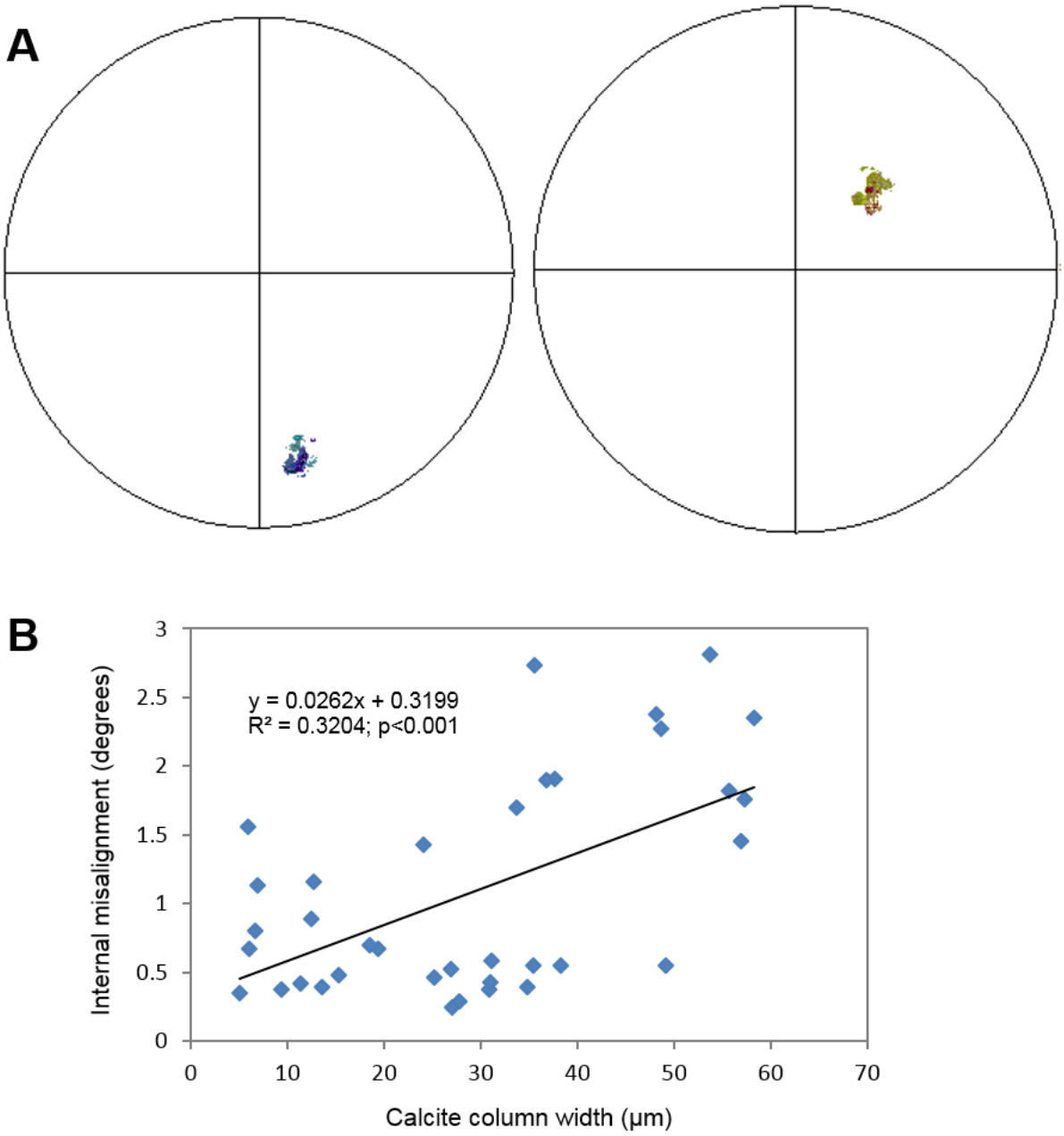

fig. S3. Internal nanocrystal misalignments in the PL of chicken eggshell. (**A**) 001 pole figure of two columnar calcite units showing a notable scattering of the *c*-axis within each column. The orientation of the *c*-axis (shown in the same pseudocolor scheme as in the EBSD maps in Fig. 2C-E) changes within a range of several degrees. (**B**) Misalignment of internal nanocrystals within a calcite column in the palisades layer as a function of size of the columns. The data indicate that there is an accumulation of defects occurring during crystal/column growth that produces an increase in the observed internal misalignment of nanocrystalline domains.

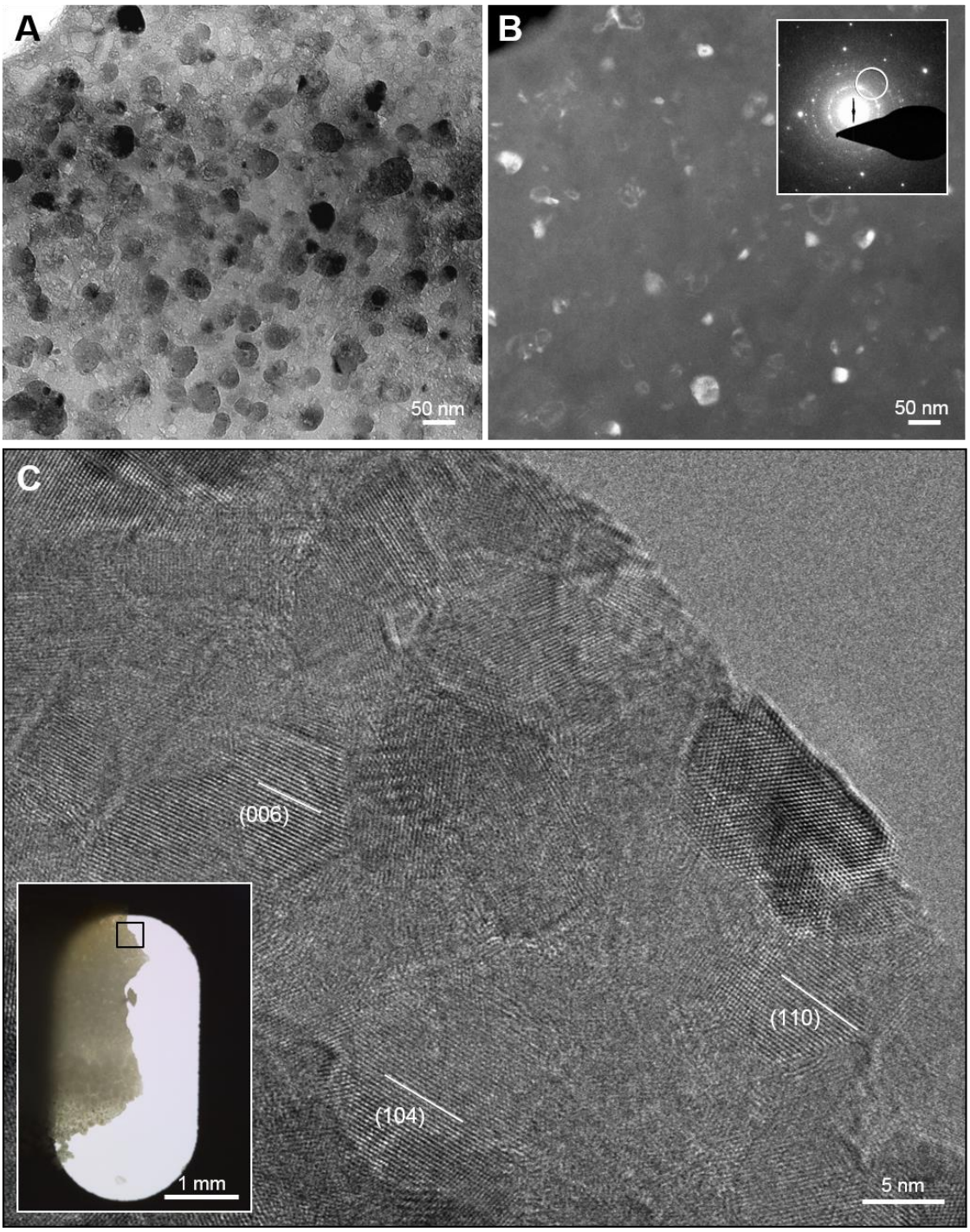

fig. S4. TEM showing eggshell nanostructure. (**A**) Bright-field and (**B**) dark-field TEM images after FIB sectioning of eggshell. Inset shows the SAED area from where the dark-field image was taken. (**C**) Mechanically prepared and polished chicken eggshell wedge cross-section (inset, low-magnification grid-mounted) showing the presence of 5-7 nm nanodomains with various indexed crystallographic orientations.

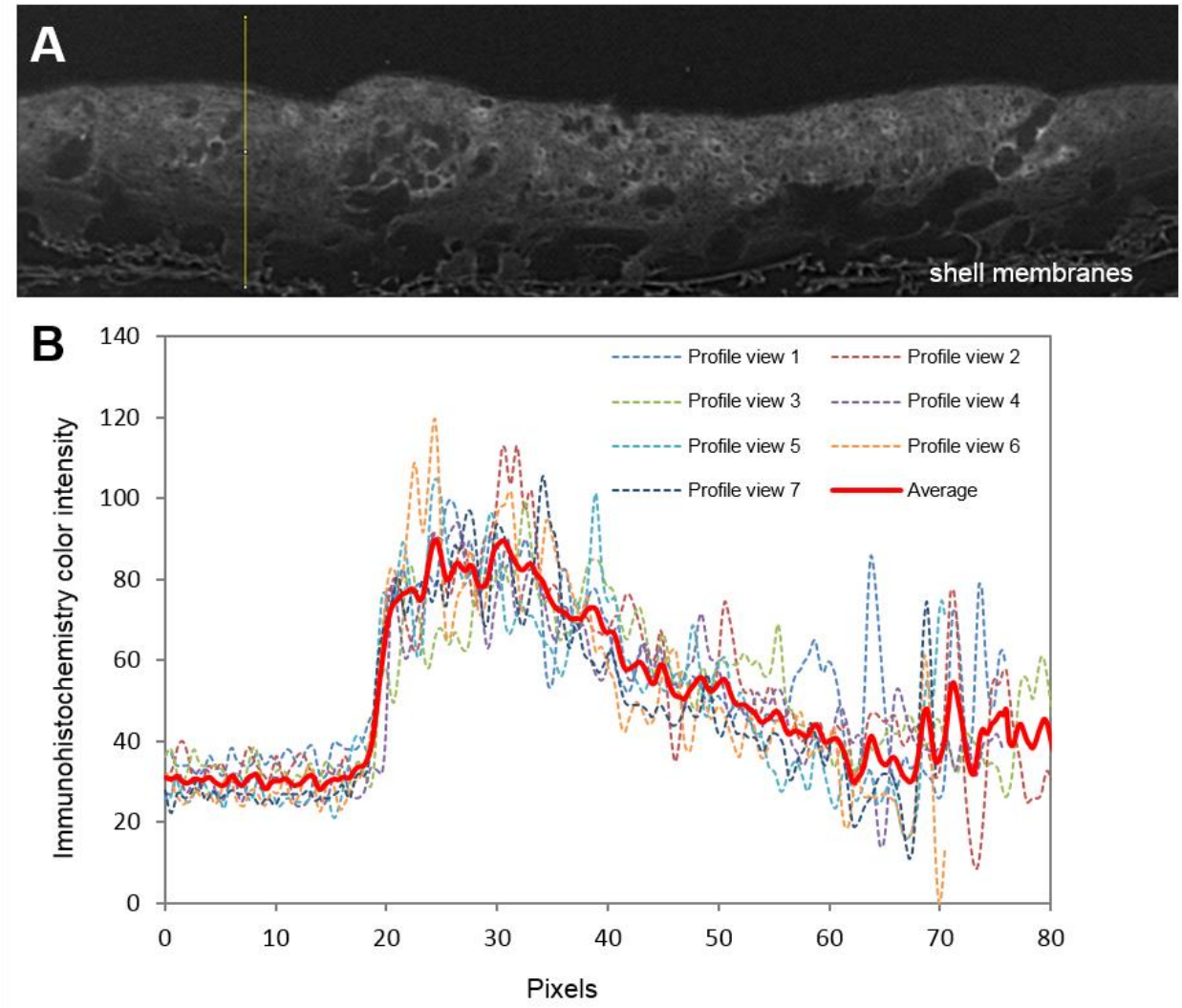

fig. S5. Semiquantification of OPN immunostaining across the eggshell thickness. (**A**) Typical profile view (vertical yellow line) from an inverted image created with ImageJ software from a digital image taken of osteopontin immunostaining of a paraffin section from a decalcified eggshell. (**B**) Plot of seven intensity profile views for osteopontin staining, with the average osteopontin intensity profile view shown in red.

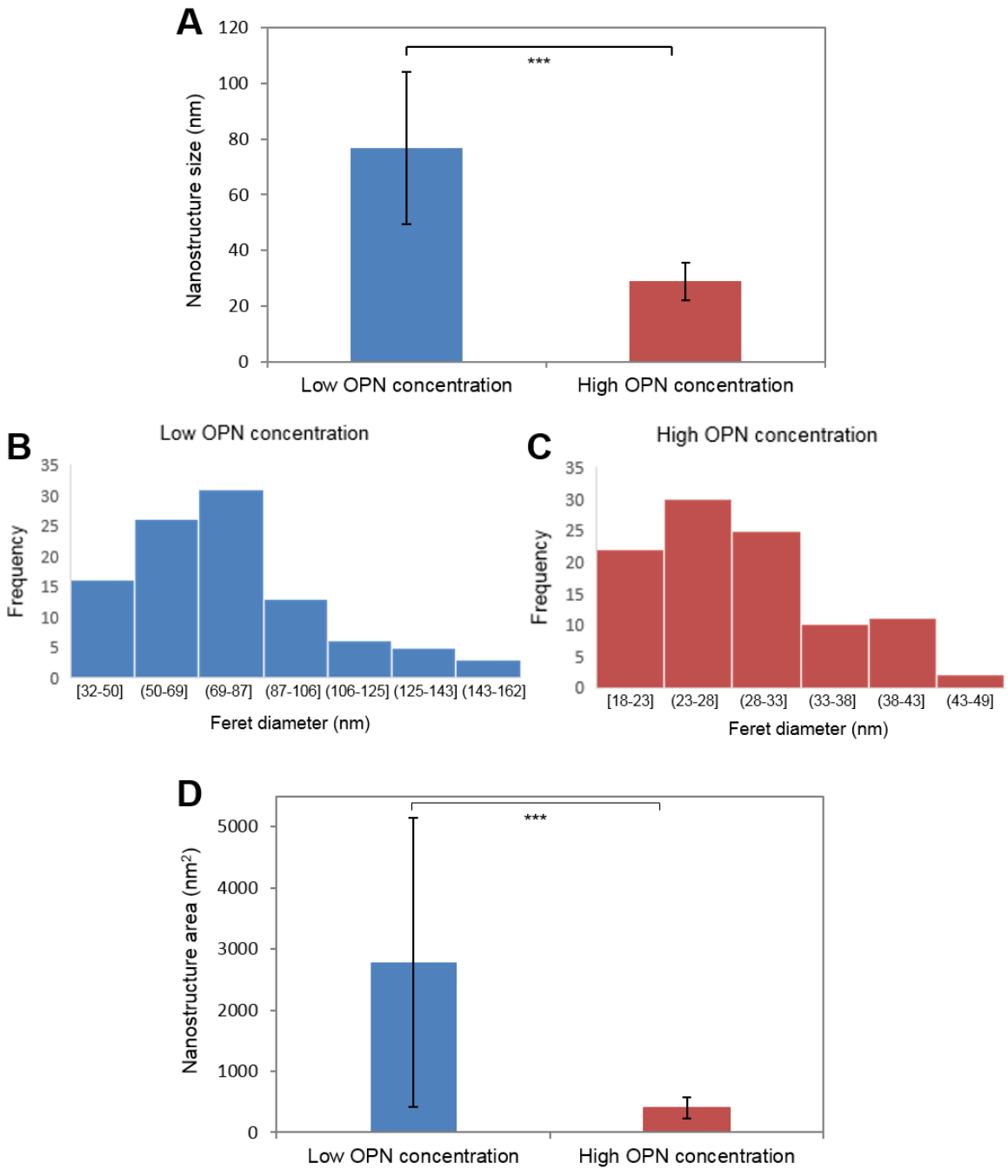

fig. S6. Effect of OPN on nanostructure size in synthetic calcite crystals. (**A**) Nanostructure size distribution between calcite crystals grown with 0.9 µM OPN or with 5.9 µM OPN. Significant difference indicated by bracket ***p<0.001. (**B** and **C**) Distribution of nanostructure in synthetic calcite crystals grown in a low (0.9 µM, B) and high (5.9 µM, C) OPN concentration. (**D**) Nanostructure area distribution of synthetic calcite crystals grown in 0.9 µM OPN or in 5.9 µM OPN. Significant difference indicated by bracket ***p<0.001. Values were compared by a two-paired Student's *t*-test.

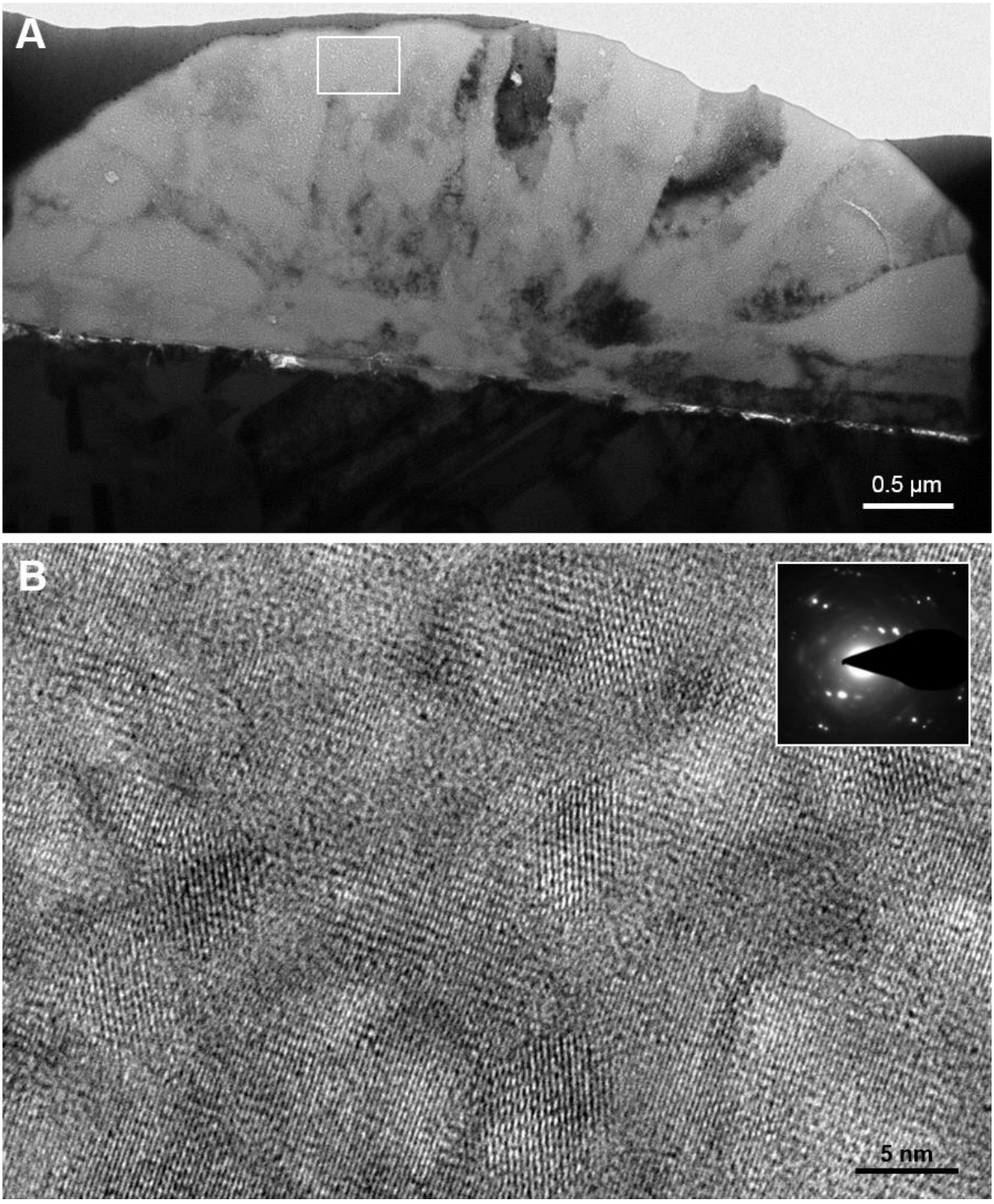

fig. S7. OPN induces nanostructure in synthetic calcite crystals. (**A**) Bright-field TEM image after FIB sectioning of a calcite crystal grown in the presence of 5.9 µM osteopontin. (**B**) HRTEM lattice imaging of the region boxed in A. Inset shows the selected-area electron diffraction pattern from this region.

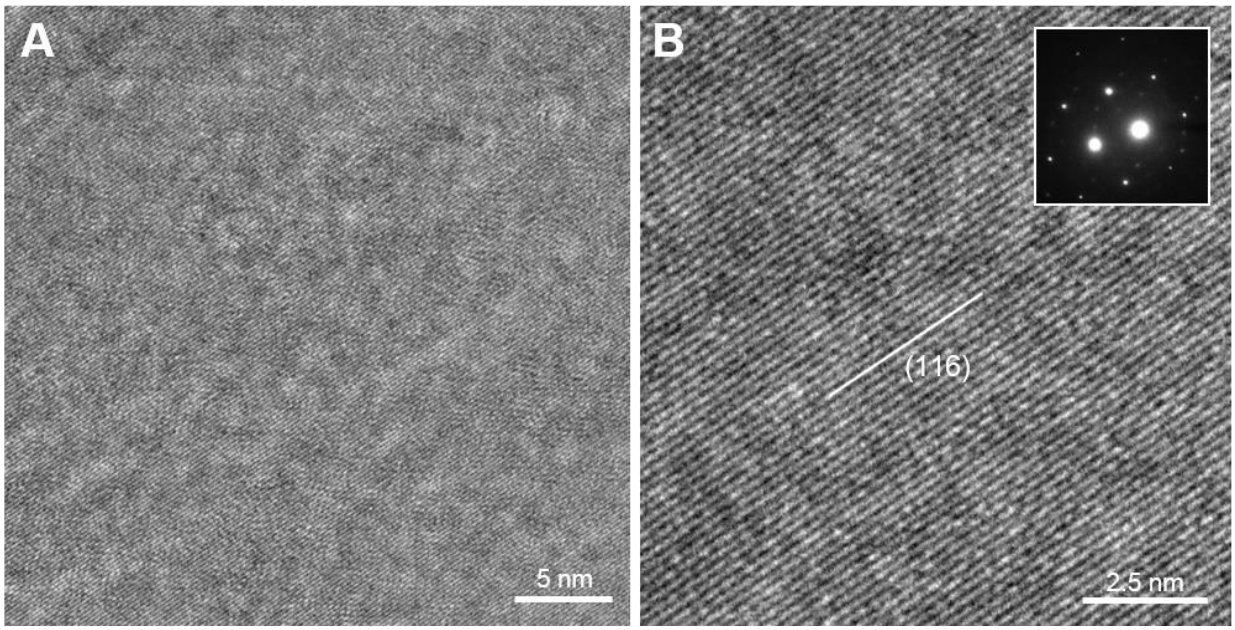

fig. S8. Absence of nanostructure in synthetic control calcite crystal (no added OPN). (**A**) Bright-field TEM image of calcite control sample after FIB sectioning showing no evidence of nanostructure. (**B**) HRTEM indexed lattice imaging of calcite control sample. Inset shows the selected-area electron diffraction pattern of the calcite showing a single crystal spot diffraction pattern.

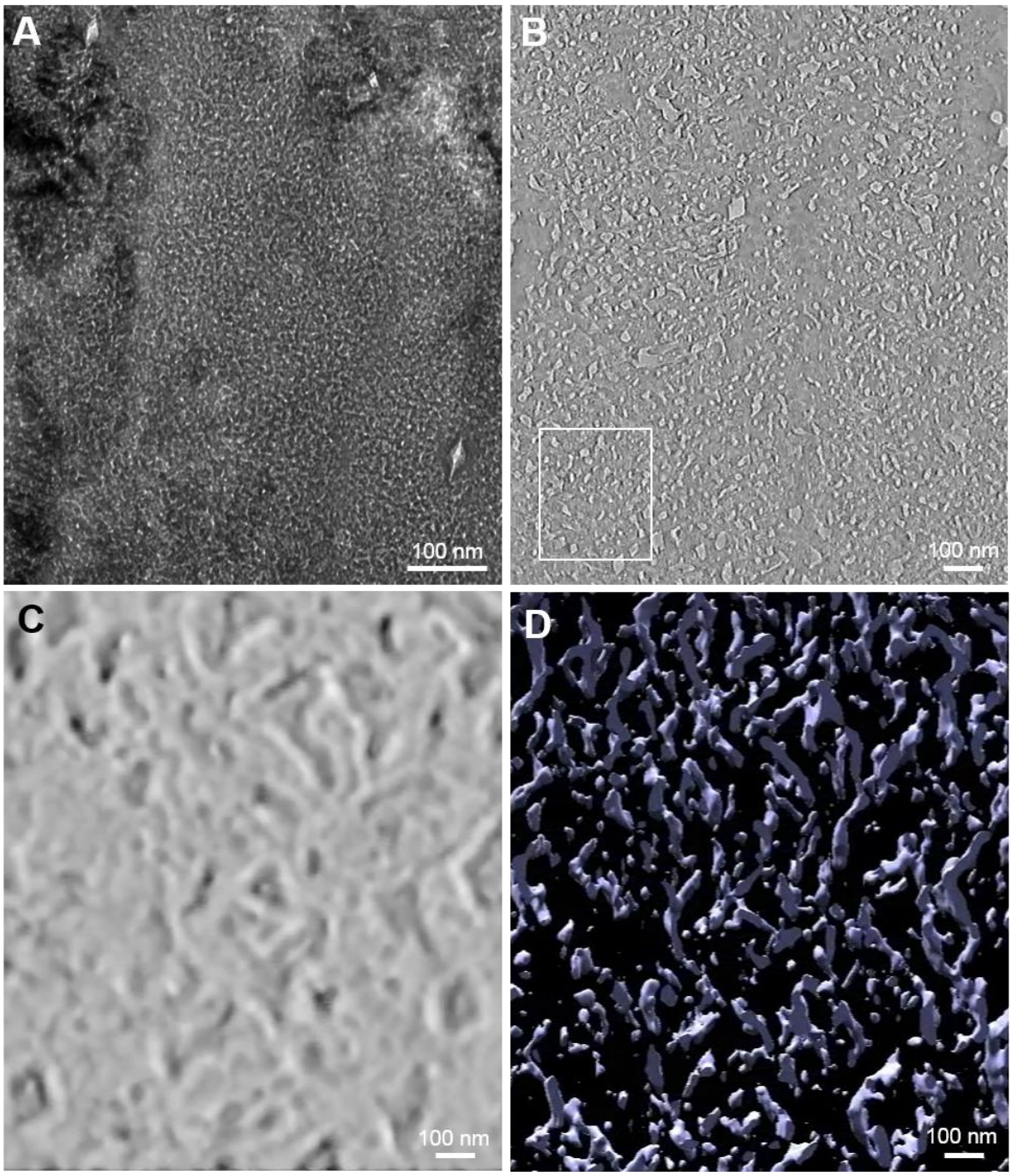

fig. S9. Electron microscopy of a FIB section showing nanostructure in a synthetic calcite crystal grown with OPN (5.9 μM). (**A**) Bright-field TEM image of a synthetic calcite crystal grown with osteopontin. (**B**) A single TEM image from the tomographic tilt series. (**C**, **D**) Three-dimensional tomographic reconstructions of the same nanostructured region indicated by the box in B (solid rendering in panel C, surface rendering in panel D). The surface rendering in panel D used a threshold that shows only high-density regions within the indicated box in panel B (see also movies S3 and S4).

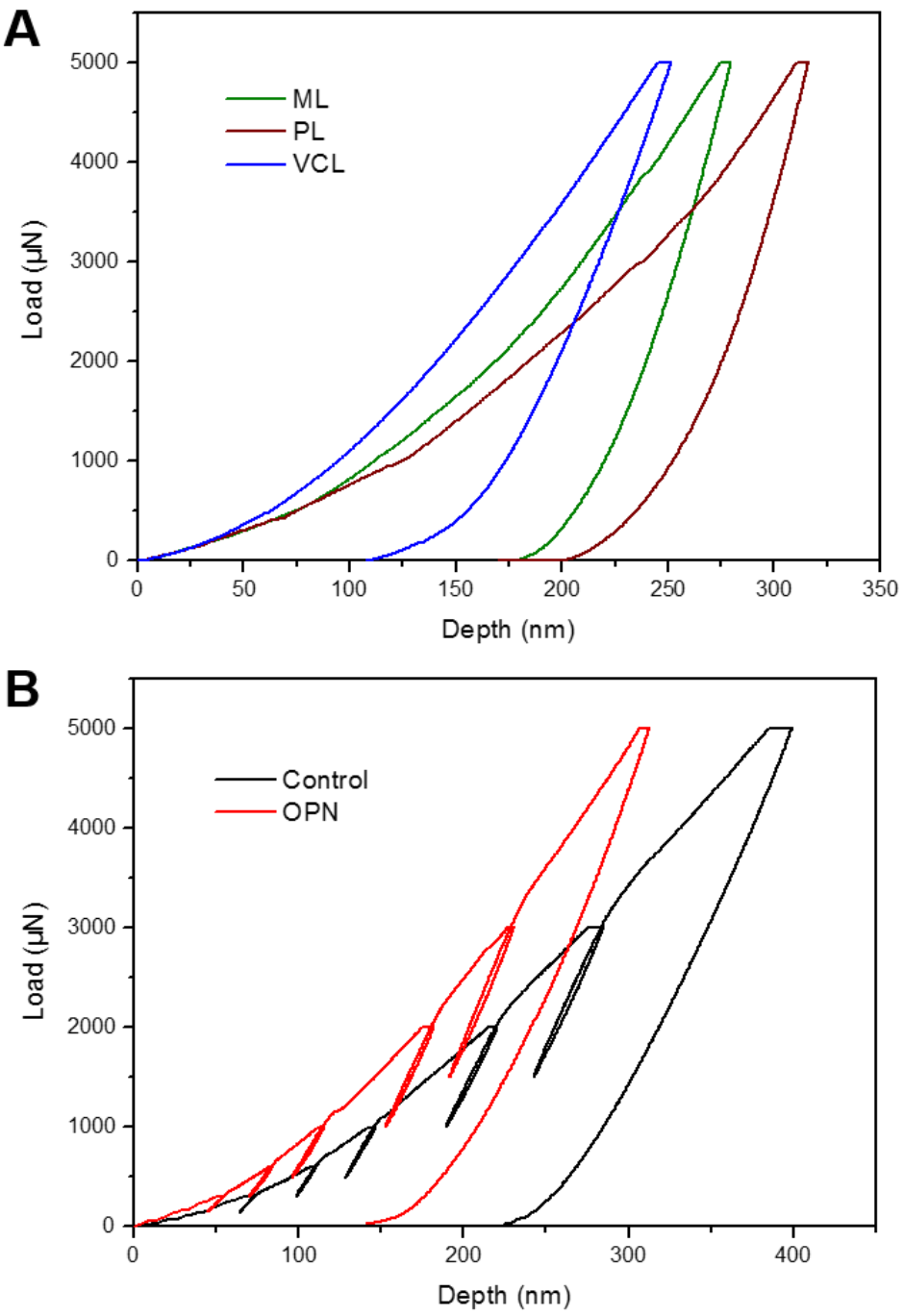

fig. S10. Nanoindentation displacement curves for eggshell and synthetic calcite crystals grown in OPN (5.9 μM). (**A**) Representative load-displacement curves from the VCL, PL (lower) and ML layers. (**B**) Partial unloading-displacement curves from synthetic calcite crystals grown with and without osteopontin.